ADVANCED FUNCTIONAL MATERIALS
www.afm-journal.de

33% Giant Anomalous Hall Current Driven by Both Intrinsic and Extrinsic Contributions in Magnetic Weyl Semimetal $Co_3Sn_2S_2$

*Jianlei Shen, Qingqi Zeng, Shen Zhang, Hongyi Sun, Qiushi Yao, Xuekui Xi, Wenhong Wang, Guangheng Wu, Baogen Shen, Qihang Liu, and Enke Liu**

The anomalous Hall effect (AHE) can be induced by intrinsic mechanisms due to the band Berry phase and extrinsic one arising from the impurity scattering. The recently discovered magnetic Weyl semimetal $Co_3Sn_2S_2$ exhibits a large intrinsic anomalous Hall conductivity (AHC) and a giant anomalous Hall angle (AHA). The predicted energy dependence of the AHC in this material exhibits a plateau at 1000 Ω^{-1} cm^{-1} and an energy width of 100 meV just below E_F, thereby implying that the large intrinsic AHC will not significantly change against small-scale energy disturbances such as slight *p*-doping. Here, the extrinsic contribution is successfully triggered from alien-atom scattering in addition to the intrinsic one of the pristine material by introducing a small amount of Fe dopant to substitute Co in $Co_3Sn_2S_2$. The experimental results show that the AHC and AHA can be prominently enhanced up to 1850 Ω^{-1} cm^{-1} and 33%, respectively, owing to the synergistic contributions from the intrinsic and extrinsic mechanisms as distinguished by the TYJ model. In particular, the tuned AHA exhibits a record value among known magnetic materials in low fields. This study opens up a pathway to engineer giant AHE in magnetic Weyl semimetals, thereby potentially advancing the topological spintronics/Weyltronics.

1. Introduction

As an important electronic phenomenon, the anomalous Hall effect (AHE) has attracted extensive research attention from the perspectives of fundamental physics and technical applicability.[1–3] Large AHE are essential for applications such as AHE sensors[4] and those based on spin-transfer torque.[5] As per current knowledge, it is believed that AHE originates from two different microscopic mechanisms, that is, intrinsic and extrinsic ones. As regards the intrinsic mechanism, Karplus and Luttinger first proposed that the spin–orbit interaction together with interband mixing results in an anomalous electron velocity in the direction transverse to the electric field;[6] this mechanism was recently revived based on the framework of Berry curvature,[6–9] which yields the resistivity relation $\rho_H \propto \rho_{xx}^2$. As regards the extrinsic mechanism, Smit and Berger proposed skew scattering and side-jump effects in the scattering process that is affected by the spin–orbit interaction, which yield the relations $\rho_H \propto \rho_{xx}$ and $\rho_H \propto \rho_{xx}^2$, respectively.[10,11] However, a large number of theoretical calculations and experimental measurements indicate that the intrinsic contribution is the dominant cause for large AHE in most materials.[12,13] Therefore, a large AHE can be expected in materials with strong Berry curvature. In particular, in magnetic Weyl materials, strong Berry curvature can be induced by Weyl nodes and gapped nodal lines engendered by the spin–orbit interaction.[14–16]

J. Shen, Q. Zeng, S. Zhang, Dr. X. Xi, Prof. W. Wang, Prof. G. Wu, Prof. B. Shen, Dr. E. Liu
State Key Laboratory for Magnetism
Institute of Physics
Chinese Academy of Sciences
Beijing 100190, China
E-mail: ekliu@iphy.ac.cn

J. Shen, Q. Zeng, S. Zhang
School of Physical Sciences
University of Chinese Academy of Sciences
Beijing 100049, China

The ORCID identification number(s) for the author(s) of this article can be found under https://doi.org/10.1002/adfm.202000830.

Dr. H. Sun, Dr. Q. Yao, Prof. Q. Liu
Shenzhen Institute for Quantum Science and Technology and Department of Physics
Southern University of Science and Technology (SUSTech)
Shenzhen 518055, China

Prof. W. Wang, Dr. E. Liu
Songshan Lake Materials Laboratory
Dongguan 523808, China

Prof. Q. Liu
Guangdong Provincial Key Laboratory for Computational Science and Material Design
Southern University of Science and Technology
Shenzhen 518055, China

DOI: 10.1002/adfm.202000830

Recently, topologically enhanced Berry curvature has been exploited to achieve intrinsic giant anomalous Hall conductivity (AHC, ≈1130 Ω^{-1} cm^{-1}) and anomalous Hall angle (AHA, ≈20%) in the magnetic Weyl semimetal $Co_3Sn_2S_2$,[17] in which the Weyl nodes, located only 60 meV above the Fermi level (E_F), act as magnetic monopoles and sources of Berry curvature, a form of pseudo-magnetic field in momentum space. Moreover, both angle-resolved photoemission spectroscopy (ARPES) and scanning tunneling spectroscopy (STM) have been used to confirm the existence of the Weyl phase.[18,19] The AHC measured in experiments is consistent with that of theoretical calculations from the band-structure Berry curvature, which indicates that the AHC mostly originates from the intrinsic component in $Co_3Sn_2S_2$.

However, the extrinsic contributions to AHE can be remarkable in certain systems. For example, in the topological ferromagnet Fe_3Sn_2, the extrinsic contribution can be five times larger than the intrinsic one.[20] In addition, a transition from intrinsic AHE to the extrinsic one has been reported in the magnetic Weyl semimetal candidate $PrAlGe_{1-x}Si_x$ for $x > 0.5$.[21] Furthermore, the magnetic Weyl system Co_2MnGa also shows a large AHC (1530 Ω^{-1} cm^{-1}), in which the extrinsic component accounts for nearly 50% of the AHC.[22] These results indicate that the extrinsic mechanism can also significantly contribute to the total AHE. Nevertheless, these reported systems still exhibit a relatively low AHA of <12%. Microscopically, the extrinsic mechanism is related to disorder scattering from the spin–orbit interaction of conduction electrons and impurities, and it strongly depends on factors such as crystal defects, impurity concentration, and film thickness.[23–27] Thus, the desired AHC and AHA can be enhanced by extrinsic contributions from suitable impurities.

2. Design Scheme

To obtain enhanced AHE, in this study, we propose a scheme to induce the extrinsic component based on the intrinsic one in the magnetic Weyl semimetal $Co_3Sn_2S_2$. In this system,[17] the strong Berry curvature is dominated by the relatively clean topological bands around the EF, including the Weyl nodes and gapped nodal lines from cobalt (Co) orbits, which produces a significant transverse Hall transport effect on the Co kagome lattices. As per our previous work,[17] the energy-dependent AHC calculated from the Berry curvature exhibits a clear peak plateau, which remains above 1000 Ω^{-1} cm^{-1} and shows an energy width of 100 meV just below E_F, as indicated by the green line in **Scheme 1**. This result implies that the contribution of the intrinsic mechanism to AHC will not significantly change against small-scale energy disturbances such as temperature change or *p*-doping. Thus, we can exploit this feature of the magnetic Weyl semimetal $Co_3Sn_2S_2$ and further dope a small amount of alien atoms onto the Co kagome lattices. In the case of Fe, which has one less valence electron than Co, it is possible to maintain the EF within the energy range of the AHC plateau (black dashed line and black arrow in Scheme 1). Simultaneously, the asymmetric scattering of moving electrons due to Fe dopants can result in the extrinsic contribution (red dashed line and red arrows in Scheme 1) in addition to the large intrinsic component. In this scheme, a magnetic Weyl semimetal with clean topological bands and high AHE is necessary as it can provide an ideal platform to manipulate the extrinsic mechanism to simultaneously enhance AHC and AHA. Therefore, we selected $Co_3Sn_2S_2$ as the platform and substituted Co atoms with a small amount of Fe atoms, corresponding to the chemical formula of $Co_{3-x}Fe_xSn_2S_2$. Here, we note that Fe atoms will directly occupy Co sites in the kagome lattices in the system.

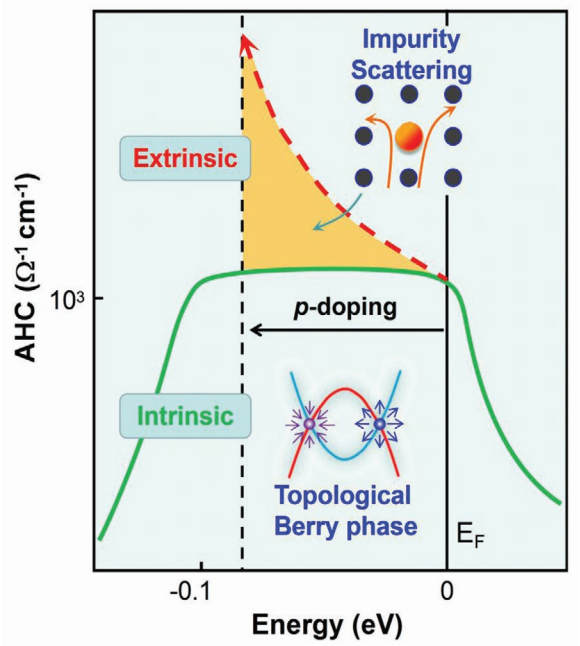

Scheme 1. Schematic for tuning AHE via controlling intrinsic and extrinsic contributions in magnetic Weyl semimetal $Co_3Sn_2S_2$. The green line denotes the intrinsic AHC of $Co_3Sn_2S_2$ dominated by the Berry phase from the topological Weyl bands. The red dashed line and orange area correspond to the extrinsic AHC from impurity scattering, respectively, generated by the slight *p*-doping of alien atoms.

3. Results and Discussion

3.1. Basic Behaviors of Magnetism and Electricity after Fe Doping

A series of $Co_{3-x}Fe_xSn_2S_2$ (x = 0, 0.025, 0.05, 0.10, 0.15, 0.20) single crystals were grown using Sn and Pb mixed flux.[28] The chemical compositions of the grown crystals were determined using energy dispersive X-ray spectroscopy (EDS) (Figure S1 and Table S1, Supporting Information). **Figure 1**a shows the crystal structure of $Co_3Sn_2S_2$. The crystal (space group R-3m) contains a quasi-2D Co–Sn kagome layer sandwiched between S and Sn atoms and stacks in the ABC fashion along the *c*-axis. The magnetic moments of Co atoms are fixed on the kagome layer in the *ab*-plane and along the *c*-axis.[29] The room-temperature X-ray diffraction (XRD) patterns of $Co_{3-x}Fe_xSn_2S_2$ show only the (000*l*) Bragg peaks, which indicates that the exposed plane surface is the *ab*-plane, as shown in Figure 1b. Moreover, the peaks (000*l*) shift to lower diffraction angles with increase in the Fe content, as illustrated in inset of Figure 1b. This indicates that

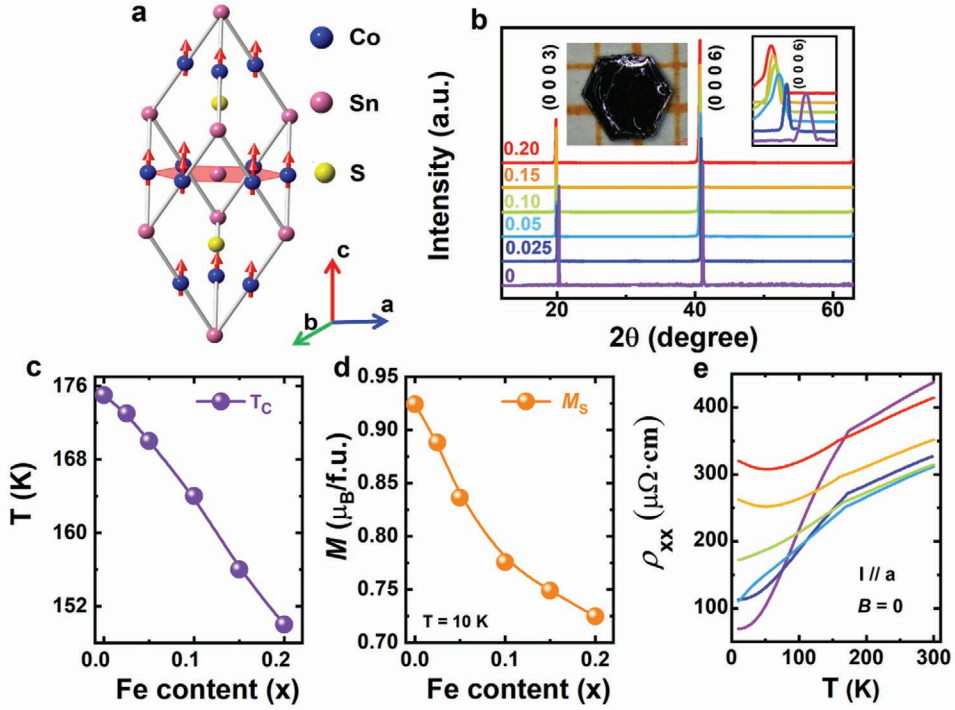

Figure 1. Crystal structure, Curie temperature (T_C), saturation magnetization (M_S), and longitudinal resistivity (ρ_{xx}) of Fe-doped $Co_{3-x}Fe_xSn_2S_2$. a) Crystal structure of $Co_3Sn_2S_2$. b) XRD patterns of $Co_{3-x}Fe_xSn_2S_2$ single crystals at room temperature. The insets show a photograph of the $Co_3Sn_2S_2$ single crystal and a zoom-in figure on the angle scale for (0006) Bragg peaks. c) T_C of $Co_{3-x}Fe_xSn_2S_2$. d) M_S of $Co_{3-x}Fe_xSn_2S_2$. e) ρ_{xx} of $Co_{3-x}Fe_xSn_2S_2$ at zero field for I // *a*.

the lattice constant increases because the radius of the Fe atom is larger than that of Co. Figure 1c,d show the Fe-content dependencies of the Curie temperature (T_C) and 10-K saturation magnetization (M_S) obtained from $M(T)$ and $M(B)$, respectively (Figure S2a,b, Supporting Information). Parameter T_C monotonously decreases from 175 K at $x = 0$ to 150 K at $x = 0.20$. Parameter M_S also monotonously reduces from 0.92 μ_B/f.u. at $x = 0$ to 0.72 μ_B/f.u. at $x = 0.20$. Both these parameters decrease with increase in the Fe doping amount, which is mainly attributed to the weaker magnetic exchange of Fe relative to Co. Figure 1e shows the longitudinal resistivity ρ_{xx} of $Co_{3-x}Fe_xSn_2S_2$ at zero field for I // *a*. All the curves exhibit a kink point corresponding to T_C, determined upon deriving the ρ_{xx} curves (see details in Figure S2c, Supporting Information). Furthermore, the samples at $x = 0.15$ and 0.20 demonstrate the Kondo effect[30,31] below 50 K, which is caused by the magnetic scattering due to the presence of the doped magnetic element Fe.

3.2. Fe-Doping Dependence of AHE

Figure 2a shows Hall resistivity ρ_{yx} as a function of magnetic field B at 10 K for B // c and I // *a*. The anomalous Hall resistivity ρ_{yx}^{A} at 10 K is obtained at zero field. We plot ρ_{yx}^{A} and ρ_{xx} as functions of the Fe content in Figure 2b. With increase in the Fe doping amount, ρ_{yx}^{A} increases gradually from 4 μΩ cm at $x = 0$ to 98 μΩ cm at $x = 0.20$, corresponding to an increment of two orders in amplitude. This giant ρ_{yx}^{A} value is seldom observed in AHE materials, particularly in single-crystalline materials. Parameter ρ_{xx} increases gradually from 69 μΩ cm at $x = 0$ to 320 μΩ cm at $x = 0.20$ at 10 K, which is caused by the enhancement of impurity scattering upon Fe doping. Furthermore, AHC σ_{xy}^{A} can be calculated from ρ_{xx} and ρ_{yx} via the relation $\sigma_{xy}^{A} = -\sigma_{yx}^{A} = \rho_{yx}/(\rho_{yx}^2 + \rho_{xx}^2)$, as shown in Figure 2c. Parameter σ_{xy}^{A} shows an initial increment and then decreases with increase in the Fe doping amount, exhibiting a maximum of 1850 Ω^{-1} cm^{-1} at $x = 0.05$, which is nearly twice as large as that of undoped $Co_3Sn_2S_2$. In addition, the AHA characterized by $\sigma_{xy}^{A}/\sigma_{xx}$ is also an important measure to describe the transport properties of AHE materials, and it reflects the efficiency of the conversion of longitudinal current into transverse current, for example, anomalous Hall current. The AHA at 10 K also demonstrates a similar Fe-doping dependence, as shown in Figure 2d, exhibiting a maximum of ≈33% at $x = 0.15$ at zero field, which is considerably larger than that of any magnetic bulk material reported previously.

Figure 2e shows the temperature dependence of the AHC at 1 kOe (larger than the out-of-plane saturation field of 0.9 kOe)[29] from 10 to 300 K (also see Figure S3, Supporting Information). As the AHC at $x = 0$ is basically dominated by the Berry curvature of the topological band structures, the AHC remains unchanged below 100 K.[17] With further increase in temperature, the increase in thermal disturbance initiates the random arrangement of magnetic moments, which reduces the strength of the Berry curvature and AHC.[17,32,33] Above T_C, the AHC disappears because the magnetic moment is completely disordered. For $x =$ 0.025, 0.05, 0.10, 0.15, and 0.20, the AHC decreases with increase in temperature, which will be discussed later in the paper.

The AHA strongly depends on the synergetic change of σ_{xy}^{A} and σ_{xx} (Figure S4, Supporting Information). For $x = 0$, the topologically protected σ_{xy}^{A} is relatively robust against temperature in low temperatures. In contrast, the σ_{xx} is sensitive

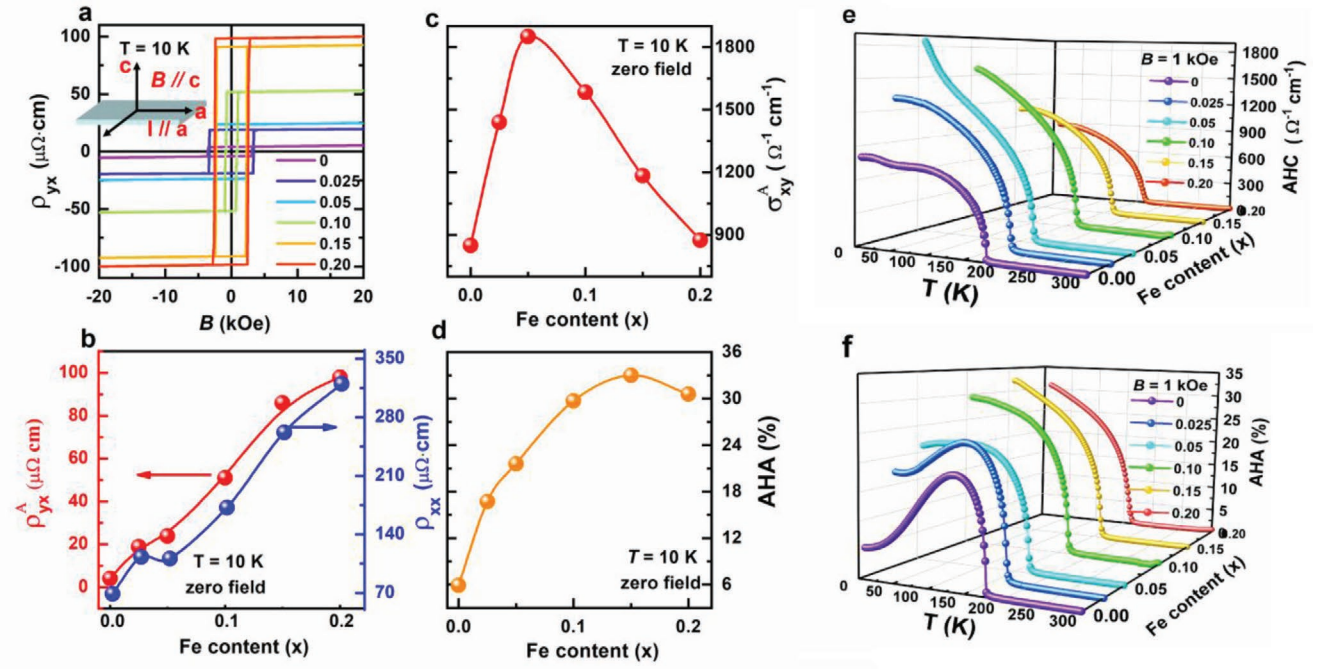

Figure 2. AHE subsequent to Fe doping. a) Hall resistivity ρ_{yx} as a function of magnetic field B at 10 K for B// c and I // a. b) Fe-doping dependences of anomalous Hall resistivity ρ_{yx}^{A} and longitudinal resistivity ρ_{xx}. c) and d) Fe-doping dependences of AHC σ_{xy}^{A} and AHA, respectively, at 10 K and zero field. e,f) Temperature dependence of AHC and AHA values of $Co_{3-x}Fe_xSn_2S_2$ at a field of 1 kOe.

to temperature owing to electron–phonon scattering and decreases rapidly with the increase of temperature. Therefore, The AHA increases gradually with the increase of temperature. However, with the further increase of temperature, the σ_{xy}^{A} decreases significantly, leading to the decrease of the AHA and showing a maximum of 19% at 135 K. The AHA of $x = 0.025$ shows the same trend like that of $x = 0$, showing a maximum of 23.6% at 110 K. For the AHA of $x = 0.05$, because both σ_{xy}^{A} and σ_{xx} decrease at low temperatures with the increase of temperature, the AHA basically keeps at ≈22% unchanged within the range of 100 K. For the AHA of $x = 0.10$, 0.15, and 0.20, the σ_{xy}^{A} decreases significantly with the increase of temperature, while the change of the σ_{xx} is not significant. Therefore, the AHAs of $x = 0.10$, 0.15, and 0.20 decrease with increase of the temperature, showing a maximum ≈30%, ≈33%, and ≈31%, respectively, at 10 K. It should be noted here that the AHC and AHA are very large over a wide temperature range.

3.3. Separation of Intrinsic and Extrinsic Mechanisms via Application of TYJ Model

Till now, we have obtained higher measured values of AHC and AHA than those of undoped $Co_3Sn_2S_2$. To verify that the enhanced AHE in $Co_{3-x}Fe_xSn_2S_2$ is caused by the increase in the extrinsic contribution, we require an effective model for separating the intrinsic and extrinsic contributions. It is generally accepted that the total σ_{xy}^{A} can be expressed as the sum of three terms: $\sigma_{xy}^{A} = \sigma_{int} + \sigma_{sk} + \sigma_{sj}$, where σ_{int}, σ_{sk}, and σ_{sj} denote the intrinsic, skew, and side-jump contributions, respectively. In this regard, Tian et al. proposed the following scaling model of the AHE, $\rho_{yx}^{A} = a\rho_{xx0} + b\rho_{xx}^{2}$. This is the so-called TYJ scaling,[27] which has been used to successfully distinguish these three contributions in many systems.[34–39] In the equation, ρ_{xx0} denotes the residual resistivity. In the TYJ scaling model, the first term on the right-hand side of the equation corresponds to the extrinsic contributions, which include the skew and side-jump components. The second term corresponds to the intrinsic contribution. The TYJ scaling can also be expressed in the conductivity form as follows, $\sigma_{xy}^{A} = -a\sigma_{xx0}^{-1}\sigma_{xx}^{2} - b$, where $\sigma_{xx0} = 1/\rho_{xx0}$ denotes the residual conductivity.

Figure 3a shows the σ_{xy}^{A} versus σ_{xx}^{2} curves for $x \le 0.10$ for the temperature range of 10–40 K (also see Figure S5, Supporting Information). We note that each curve can be fitted by a linear relationship. The intercept b of each line on the longitudinal axis represents the intrinsic AHC contribution. In order to display the fitting accuracy clearly, the fitting result of $x = 0.05$ as a representative is also shown in Figure S6 of Supporting Information. Next, we separated the results into the extrinsic and intrinsic components at 10 K by applying the TYJ model, where $\sigma_{xx0} \approx \sigma_{xx}(10K)$, as shown in Figure 3b. It can be observed that the intrinsic σ_{xy}^{A} (int.) basically lies between 850 and 1000 Ω^{-1} cm^{-1} with slight variations when $x = 0$, 0.025, 0.05. This result confirms that the intrinsic contribution to AHC does not change for small amounts of Fe p-doping in $Co_3Sn_2S_2$, even if the E_F value shifts slightly downward. The theoretical calculations from energy bands also reveal a consistent behavior with a slight increase (see Figure S7, Supporting Information, for details), which further indicates the reliability of the results separated by TYJ model. Importantly, both the intrinsic AHCs from experiment and theoretical calculations are basically kept at the same level of pristine $Co_3Sn_2S_2$, which confirms our claim that the E_F is still on the AHC-plateau for the low Fe-doping levels and the intrinsic AHC will not significantly change for the low p-doping.

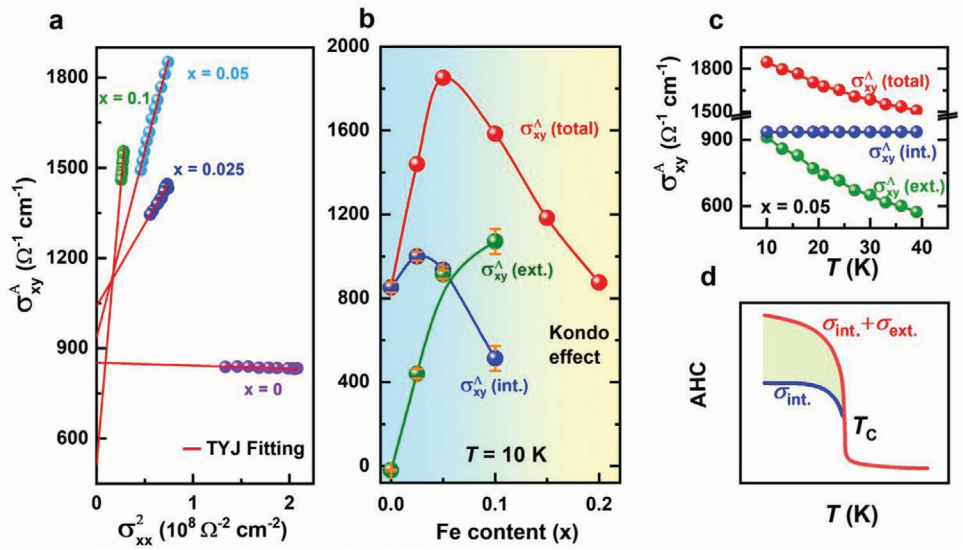

Figure 3. Scaling of AHE. a) Parameter σ^A_{xy} as function of square of longitudinal conductivity σ^2_{xx}. The solid red lines indicate the fitting results with $\sigma^A_{xy} = -a\sigma^{-1}_{xx0}\sigma^2_{xx}-b$. b) Scaling AHC data of $Co_{3-x}Fe_xSn_2S_2$ at 10 K. c) Temperature dependence of total AHC σ^A_{xy}, intrinsic σ^A_{xy}(int.), and extrinsic σ^A_{xy} (ext.) at $x = 0.05$ from 10 to 40 K at zero field. d) Schematic of the temperature dependence of σ^A_{xy}, σ^A_{xy}(int.), and σ^A_{xy}(ext.).

Meanwhile, the extrinsic σ^A_{xy}(ext.) rapidly increases from –20 Ω^{-1} cm^{-1} at $x = 0$ to 914 Ω^{-1} cm^{-1} at $x = 0.05$. It is clear that slight Fe doping can produce a large, positive extrinsic contribution in the magnetic Weyl semimetal $Co_3Sn_2S_2$, while the large intrinsic component remains as the band Berry curvature is not changed by the slight doping. Therefore, giant AHC is obtained at $x = 0.05$ owing to the dual contribution of the intrinsic and extrinsic mechanisms. However, although σ^A_{xy}(ext.) continues to increase to 1071 Ω^{-1} cm^{-1} at $x = 0.10$, the AHC begins to decrease because of the further increase in Fe content, which results in a significant decrease in E_F, which in turn corresponds to a significant decrease in the intrinsic contribution, as depicted by the intrinsic AHC line (green) in Scheme 1. As regards the origin of the extrinsic contribution for $x \le 0.10$, we make a further analysis according to $\log \rho^A_{yx} = \alpha \log \rho_{xx}$, where α denotes an exponent of ρ_{xx} (see details in Figure S8, Supporting Information). The skew and side-jump mechanisms yield relations of $\rho_H \propto \rho_{xx}$ and $\rho_H \propto \rho^2_{xx}$, respectively. With increase in Fe doping, α gradually decreases from 2 to 0.7, which indicates that the enhanced extrinsic contribution for $x \le 0.10$ is mainly due to the skew mechanism. In $Co_3Sn_2S_2$, the conduction electrons mainly originate from the bands of Co in the kagome layer. The small number of doped Fe atoms randomly occupy Co sites in the kagome lattice, which leads to asymmetric scattering of the conduction electrons due to the effective spin–orbit interaction between them. Meanwhile, Wang et al. have reported that the side-jump contribution to AHE in $Co_3Sn_2S_2$ is negligible.[33]

With further increase in Fe doping, the Kondo effect is observed at $x = 0.15$ and 0.20, which is indicated by the upwarps of the R–T curves at low temperatures, as shown in Figure 1e. Currently, no effective model can be used to separate the AHC in Kondo systems. A previous work has reported that the Kondo effect negatively contributes to AHC.[40] Moreover, a further increase in Fe doping leads to a large decrease in E_F, which also results in a decrease in the intrinsic contribution. Thus, the decrease in AHC at $x = 0.15$, 0.20 is mainly because of the decrease in E_F and the Kondo effect.

In addition, the temperature dependences of the total σ^A_{xy}, σ^A_{xy}(int.), and σ^A_{xy}(ext.) at $x = 0.05$ from 10 to 40 K at zero field are shown in Figure 3c. With increase in temperature over a small range, σ^A_{xy}(int.) remains at around 930 Ω^{-1} cm^{-1}, as discussed above. However, with increase in temperature, the phonon scattering increases and the longitudinal conductivity decreases, which reduces the extrinsic contribution with increase in temperature, as per $(-a\sigma^{-1}_{xx0}\sigma^2_{xx})$. Therefore, σ^A_{xy}(ext.) and total σ^A_{xy} decrease with increase in temperature, while σ^A_{xy}(int.) remains constant, as illustrated in Figure 3d.

3.4. Comparison of $Co_{3-x}Fe_xSn_2S_2$ with Other AHE Materials

In most materials, the AHC mainly originates from the topologically trivial electronic bands and impurity scattering. A typical feature of these materials is that both σ^A_{xy} and σ_{xx} are either large or small, and therefore, AHC and AHA are not large at the same time. Meanwhile, the magnetic Weyl semimetal $Co_3Sn_2S_2$, owing to the topological-band-structure-induced large Berry curvature and the Weyl semi-metallic character, possesses both large AHC and AHA simultaneously at zero magnetic field.[17]

Figure 4 shows the AHA and AHC for different Fe-doping levels of $Co_{3-x}Fe_xSn_2S_2$ in the temperature range from 150 to 10 K along with those of other materials measured in low magnetic fields. It is clear that the AHA and AHC values of most AHE materials are not simultaneously large, as indicated by their location in the lower left corner of the plot in Figure 4. On the contrary, both the AHC and AHA values of $Co_{3-x}Fe_xSn_2S_2$ are the largest of all AHE materials (as indicated by the plots located in the upper right corner). Moreover, it should be noted

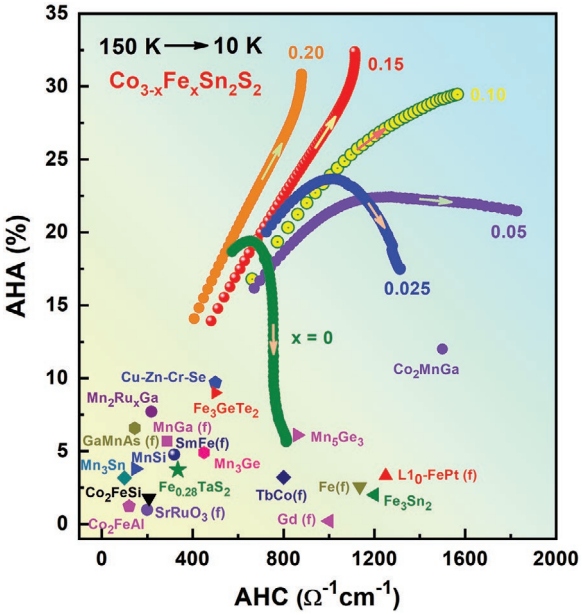

Figure 4. Comparison of AHA and AHC values of $Co_{3-x}Fe_xSn_2S_2$ with corresponding ones of other AHE materials. The data for different doping levels of $Co_{3-x}Fe_xSn_2S_2$ are shown from 150 to 10 K by means of arrows on the curves. "(f)" denotes thin-film materials. From the view of the potential applications, the applied external magnetic field for Hall response should be quite low, which means that the ground state of the material at zero field is FM or sometimes, AFM but with nonzero Berry curvature such as Mn_3Sn or Mn_3Ge. All the materials are collected based on this principle.

that the AHA at $x = 0.15$ is as high as ≈33%, which is the largest AHA of known materials previously reported in low magnetic fields. Such large values of AHC and AHA are derived by increasing the extrinsic contribution over and above the constant intrinsic contribution. Moreover, $Co_{3-x}Fe_xSn_2S_2$ can further maintain these large AHC and AHA values over a wide temperature range. The large AHA at zero field indicates that up to one-third of the longitudinal driving current can be converted to transverse current. More importantly, the huge AHA is obtained in zero field due to the low saturation field and large magnetic coercivity, which is quite different from the case of other systems showing AHA only at high fields. All of these can be greatly beneficial for potential applications such as AHE sensors[4] or those based on spin-transfer torque.[5]

4. Conclusion

In summary, we proposed a scheme to simultaneously tune the AHC and AHA to large values in the magnetic Weyl semimetal $Co_{3-x}Fe_xSn_2S_2$ by means of *p*-doping. Exploiting the fact that the large intrinsic AHC contribution in $Co_3Sn_2S_2$ is basically unchanged for slight *p*-doping, we considered that a small amount of Fe (with a lesser number of electrons relative to Co) replacing Co in the magnetic Weyl semimetal $Co_3Sn_2S_2$ can increase the extrinsic contribution via asymmetric impurity scattering. Thus, significantly enhanced AHC (≈1850 Ω^{-1} cm^{-1}) and AHA (≈33%) values were obtained in the magnetic Weyl semimetal $Co_{3-x}Fe_xSn_2S_2$, and these values persisted over a wide temperature range. Here, we note that the AHA value (≈33%) at zero field is a new record among known magnetic materials. The obtained large anomalous Hall current over a wide temperature range can be exploited for application in topological spintronics or Weyltronics. Furthermore, our study provides an effective strategy to manipulate the giant AHE via controlling the intrinsic and/or extrinsic contributions in magnetic Weyl materials.

5. Experimental Section

Single Crystal Growth: The single crystals of $Co_{3-x}Fe_xSn_2S_2$ ($0 \le x \le 0.20$) can be grown using Sn and Pb mixed flux. Co (99.95% Alfa), Fe (99.95% Alfa), Sn (99.999% Alfa), S (99.999% Alfa), and Pb (99.999% Alfa) were mixed in an initial mixture of molar ratios (Co+Fe): S: Sn: Pb = 12: 8: 35: 45. These mixtures were placed in a Al_2O_3 crucible. Then, the Al_2O_3 crucibles were sealed in quartz tubes that were put in an electric furnace. The quartz tubes were slowly heated to 673 K over 6 h and held on for extra 6 h for preventing the loss of sulfur due to the high vapor pressure. Then, the quartz tubes were heated to 1323 K over 6 h and kept there for 6 h. The melt was cooled slowly to 973 K over 70 h. At 973 K, the ampoule was removed from the electric furnace and the flux was removed via rapid decanting and subsequent spinning in a centrifuge. The single crystals of $Co_{3-x}Fe_xSn_2S_2$ with typical sizes 2–5 mm and hexagonal shape were obtained. The crystal structure and composition of single crystals were confirmed by X-ray diffraction measurements and the energy dispersive X-ray spectroscopy EDS.

Magnetization and Electric Transport Measurements: Magnetic properties were measured by superconducting quantum interference device (SQUID) magnetometer. Electric transport was measured by the physical property measurement system (PPMS).

Supporting Information

Supporting Information is available from the Wiley Online Library or from the author.

Acknowledgements

This work was supported by the National Natural Science Foundation of China (Nos. 11974394 and 51722106), the National Key R&D Program of China (Nos. 2019YFA0704904, 2017YFA0206303), the Strategic Priority Research Program (B) of the Chinese Academy of Sciences (CAS) (XDB33000000), Beijing Natural Science Foundation (No. Z190009), Users with Excellence Program of Hefei Science Center CAS (No. 2019HSC-UE009), and Fujian Institute of Innovation, CAS.

Conflict of Interest

The authors declare no conflict of interest.

Keywords

anomalous Hall angle, anomalous Hall effect, extrinsic mechanisms, intrinsic mechanisms, magnetic Weyl semimetals

Received: January 28, 2020
Revised: April 17, 2020
Published online:

[1] N. Nagaosa, J. Sinova, S. Onoda, A. H. MacDonald, N. P. Ong, *Rev. Mod. Phys.* **2010**, *82*, 1539.
[2] E. V. Vidal, G. Stryganyuk, H. Schneider, C. Felser, G. Jakob, *Appl. Phys. Lett.* **2011**, *99*, 132509.
[3] C.-Z. Chang, J. Zhang, M. Liu, Z. Zhang, X. Feng, K. Li, L.-L. Wang, X. Chen, X. Dai, Z. Fang, X.-L. Qi, S.-C. Zhang, Y. Wang, K. He, X.-C. Ma, Q.-K. Xue, *Adv. Mater.* **2013**, *25*, 1065.
[4] Y. Zhang, Q. Hao, G. Xiao, *Sensors* **2019**, *19*, 3537.
[5] S. Iihama, T. Taniguchi, K. Yakushiji, A. Fukushima, Y. Shiota, S. Tsunegi, R. Hiramatsu, S. Yuasa, Y. Suzuki, H. Kubota, *Nat. Electron.* **2018**, *1*, 120.
[6] R. Karplus, J. M. Luttinger, *Phys. Rev.* **1954**, *95*, 1154.
[7] G. Sundaram, Q. Niu, *Phys. Rev. B* **1999**, *59*, 14915.
[8] T. Jungwirth, Q. Niu, A. H. MacDonald, *Phys. Rev. Lett.* **2002**, *88*, 207208.
[9] M. Onoda, N. Nagaosa, *J. Phys. Soc. Jpn.* **2002**, *71*, 19.
[10] J. Smit, *Physica* **1958**, *24*, 39.
[11] L. Berger, *Phys. Rev. B* **1970**, *2*, 4559.
[12] Z. Fang, N. Nagaosa, K. S. Takahashi, A. Asamitsu, R. Mathieu, T. Ogasawara, H. Yamada, M. Kawasaki, Y. Tokura, K. Terakura, *Science* **2003**, *302*, 92.
[13] Y. Yao, L. Kleinman, A. H. MacDonald, J. Sinova, T. Jungwirth, D.-s. Wang, E. Wang, Q. Niu, *Phys. Rev. Lett.* **2004**, *92*, 037204.
[14] B. Yan, C. Felser, *Annu. Rev. Condens. Matter Phys.* **2017**, *8*, 337.
[15] H. Weng, C. Fang, Z. Fang, B. A. Bernevig, X. Dai, *Phys. Rev. X* **2015**, *5*, 011029.
[16] K. Manna, L. Muechler, T.-H. Kao, R. Stinshoff, Y. Zhang, J. Gooth, N. Kumar, G. Kreiner, K. Koepernik, R. Car, J. Kübler, G. H. Fecher, C. Shekhar, Y. Sun, C. Felser, *Phys. Rev. X* **2018**, *8*, 041045.
[17] E. Liu, Y. Sun, N. Kumar, L. Muchler, A. Sun, L. Jiao, S. Y. Yang, D. Liu, A. Liang, Q. Xu, J. Kroder, V. Suss, H. Borrmann, C. Shekhar, Z. Wang, C. Xi, W. Wang, W. Schnelle, S. Wirth, Y. Chen, S. T. B. Goennenwein, C. Felser, *Nat. Phys.* **2018**, *14*, 1125.
[18] D. F. Liu, A. J. Liang, E. K. Liu, Q. N. Xu, Y. W. Li, C. Chen, D. Pei, W. J. Shi, S. K. Mo, P. Dudin, T. Kim, C. Cacho, G. Li, Y. Sun, L. X. Yang, Z. K. Liu, S. S. P. Parkin, C. Felser, Y. L. Chen, *Science* **2019**, *365*, 1282.
[19] N. Morali, R. Batabyal, P. K. Nag, E. Liu, Q. Xu, Y. Sun, B. Yan, C. Felser, N. Avraham, H. Beidenkopf, *Science* **2019**, *365*, 1286.
[20] L. Ye, M. Kang, J. Liu, F. von Cube, C. R. Wicker, T. Suzuki, C. Jozwiak, A. Bostwick, E. Rotenberg, D. C. Bell, L. Fu, R. Comin, J. G. Checkelsky, *Nature* **2018**, *555*, 638.
[21] H.-Y. Yang, B. Singh, B. Lu, C.-Y. Huang, F. Bahrami, W.-C. Chiu, D. Graf, S.-M. Huang, B. Wang, H. Lin, D. Torchinsky, A. Bansil, F. Tafti, *APL Mater.* **2020**, *8*, 011111.
[22] I. Belopolski, K. Manna, D. S. Sanchez, G. Chang, B. Ernst, J. Yin, S. S. Zhang, T. Cochran, N. Shumiya, H. Zheng, B. Singh, G. Bian, D. Multer, M. Litskevich, X. Zhou, S.-M. Huang, B. Wang, T.-R. Chang, S.-Y. Xu, A. Bansil, C. Felser, H. Lin, M. Z. Hasan, *Science* **2019**, *365*, 1278.
[23] G. Bergmann, F. Ye, *Phys. Rev. Lett.* **1991**, *67*, 735.
[24] P. Mitra, N. Kumar, N. Samarth, *Phys. Rev. B* **2010**, *82*, 035205.
[25] L. Wu, K. Zhu, D. Yue, Y. Tian, X. Jin, *Phys. Rev. B* **2016**, *93*, 214418.
[26] D. Hou, G. Su, Y. Tian, X. Jin, S. A. Yang, Q. Niu, *Phys. Rev. Lett.* **2015**, *114*, 217203.
[27] Y. Tian, L. Ye, X. Jin, *Phys. Rev. Lett.* **2009**, *103*, 087206.
[28] M. A. Kassem, Y. Tabata, T. Waki, H. Nakamura, *J. Solid State Chem.* **2016**, *233*, 8.
[29] J. Shen, Q. Zeng, S. Zhang, W. Tong, L. Ling, C. Xi, Z. Wang, E. Liu, W. Wang, G. Wu, B. Shen, *Appl. Phys. Lett.* **2019**, *115*, 212403.
[30] V. Dobrosavljević, T. R. Kirkpatrick, B. G. Kotliar, *Phys. Rev. Lett.* **1992**, *69*, 1113.
[31] H. Suhl, *Phys. Rev.* **1965**, *138*, A515.
[32] Z. Guguchi, J. Verezhak, D. Gawryluk, S. Tsirkin, J. Yin, I. Belopolski, H. Zhou, G. Simutis, S. Zhang, T. Cochran, G. Chang, E. Pomjakushina, L. Keller, Z. Skrzeczkowska, Q. Wang, H. Lei, R. Khasanov, A. Amato, S. Jia, T. Neupert, H. Luetkens, M. Hasan, *Nat. Commun.* **2020**, *11*, 559.
[33] Q. Wang, Y. Xu, R. Lou, Z. Liu, M. Li, Y. Huang, D. Shen, H. Weng, S. Wang, H. Lei, *Nat. Commun.* **2018**, *9*, 3681.
[34] L. Ye, Y. Tian, X. Jin, D. Xiao, *Phys. Rev. B* **2012**, *85*, 220403.
[35] D. Hou, Y. Li, D. Wei, D. Tian, L. Wu, X. Jin, *J. Phys.: Condens. Matter* **2012**, *24*, 482001.
[36] L. Wu, Y. Li, J. Xu, D. Hou, X. Jin, *Phys. Rev. B* **2013**, *87*, 155307.
[37] J. Xu, Y. Li, D. Hou, L. Ye, X. Jin, *Appl. Phys. Lett.* **2013**, *102*, 162401.
[38] Y. Li, D. Hou, L. Ye, Y. Tian, J. Xu, G. Su, X. Jin, *Europhys. Lett.* **2015**, *110*, 27002.
[39] G. Su, Y. Li, D. Hou, X. Jin, H. Liu, S. Wang, *Phys. Rev. B* **2014**, *90*, 214410.
[40] L. J. Zhu, S. H. Nie, J. H. Zhao, *Phys. Rev. B* **2016**, *93*, 195112.